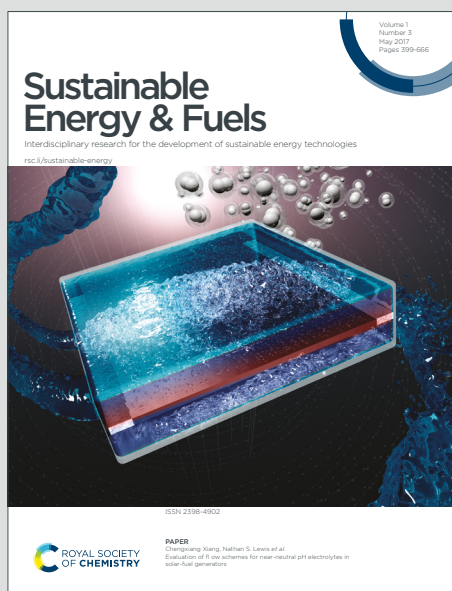


# Sustainable Energy & Fuels

Interdisciplinary research for the development of sustainable energy technologies

Accepted Manuscript

This article can be cited before page numbers have been issued, to do this please use: T. Higo, S. Ishizaki, K. Ichizuka and Y. Sekine, *Sustainable Energy Fuels*, 2026, DOI: 10.1039/D6SE00152A.



This is an Accepted Manuscript, which has been through the Royal Society of Chemistry peer review process and has been accepted for publication.

Accepted Manuscripts are published online shortly after acceptance, before technical editing, formatting and proof reading. Using this free service, authors can make their results available to the community, in citable form, before we publish the edited article. We will replace this Accepted Manuscript with the edited and formatted Advance Article as soon as it is available.

You can find more information about Accepted Manuscripts in the [Information for Authors](#).

Please note that technical editing may introduce minor changes to the text and/or graphics, which may alter content. The journal's standard [Terms & Conditions](#) and the [Ethical guidelines](#) still apply. In no event shall the Royal Society of Chemistry be held responsible for any errors or omissions in this Accepted Manuscript or any consequences arising from the use of any information it contains.

# Improved reverse water-gas shift chemical looping performance of Co-In-based oxygen carriers supported on ceria

**Author:** Takuma Higo<sup>†\*</sup>, Shuhei Ishizaki<sup>†</sup>, Kenji Ichizuka<sup>†</sup>, Yasushi Sekine<sup>†\*</sup>

## Affiliation:

<sup>†</sup> Department of Applied Chemistry, Waseda University, 3-4-1, Okubo, Shinjuku, Tokyo, 169-8555, Japan

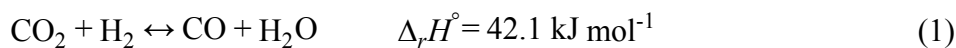
\*Correspondence to: thigo.catal@gmail.com, ysekine@waseda.jp

## Abstract

Indium-based oxygen carriers supported on various oxides were evaluated for the reverse water-gas shift chemical looping (RWGS-CL) at 773 K. Among the materials investigated, 20wt% CoIn<sub>2</sub>/CeO<sub>2</sub> showed superior performance, achieving high CO yield and space-time yield, and stable cyclic operation. Comparative studies revealed that, under RWGS-CL conditions, In species supported on CeO<sub>2</sub> exhibited spontaneous dispersion, a behaviour not observed on other oxide supports ( $\gamma$ -Al<sub>2</sub>O<sub>3</sub>, rutile-TiO<sub>2</sub>, anatase-TiO<sub>2</sub>, and SiO<sub>2</sub>). This dispersion led to the formation of a highly dispersed In surface during operation, which is associated with enhanced CO formation through improved contact with CO<sub>2</sub>. Furthermore, Co was found to accelerate the reduction kinetics of In species, likely by promoting H<sub>2</sub> dissociation and hydrogen spillover, while exerting little influence on oxidation kinetics. These results demonstrate that support-dependent structural changes play a key role in determining RWGS-CL performance.

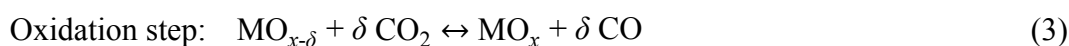
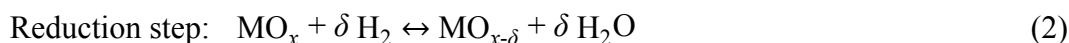
## 1. Introduction

Carbon dioxide (CO<sub>2</sub>) emissions associated with anthropogenic activities have raised serious concerns as a major contributor to global warming and related environmental issues.<sup>1,2</sup> Accordingly, the development of carbon capture and utilisation (CCU) technologies has become an urgent priority for the realisation of a decarbonised society.<sup>3</sup> Among the processes for converting captured CO<sub>2</sub> into value-added chemicals, the reverse water-gas shift (RWGS) reaction, shown in Equation (1), is recognised as one of the key reactions.<sup>4,5</sup> Carbon monoxide (CO), the main product of RWGS, is a principal component of synthesis gas and serves as an essential feedstock for a wide range of chemicals.



33 Nevertheless, conventional catalytic RWGS suffers from several inherent limitations, including the  
34 requirement for high reaction temperatures, formation of CH<sub>4</sub> as undesired by-product, and the need  
35 for costly downstream gas separation. To address these issues at a fundamental level, alternative  
36 approaches to the RWGS reaction are required.<sup>4-6</sup>

37 Reverse water-gas shift chemical looping (RWGS-CL) is regarded as a highly promising extended  
38 RWGS process that can fundamentally overcome the intrinsic limitations of conventional catalytic  
39 RWGS systems.<sup>7-9</sup> RWGS-CL consists of the following two sequential reaction steps.



42 In the reduction step, the metal oxide (MO<sub>x</sub>) is reduced by H<sub>2</sub>, followed by the oxidation step, in which  
43 the reduced metal oxide (MO<sub>x-δ</sub>) reacts with CO<sub>2</sub> to regenerate MO<sub>x</sub> and produce CO. Continuous CO  
44 production is achieved through repeated operation of this two-step cycle. The metal oxide that shuttle  
45 between these two spatially or temporally separated reactions is referred to as oxygen carrier (OC). By  
46 decoupling the reduction and oxidation reactions, RWGS-CL circumvents the thermodynamic  
47 limitations of conventional catalytic RWGS, undesired CH<sub>4</sub> formation, and lowers downstream  
48 separation costs by simplifying the composition of the outlet gas. In addition to these advantages, the  
49 stepwise redox operation in RWGS-CL fundamentally differs from conventional catalytic RWGS,  
50 where H<sub>2</sub> and CO<sub>2</sub> coexist in the same reaction environment. In RWGS-CL, the temporal separation  
51 of reduction and oxidation steps allows the redox-active species to dynamically change their structure  
52 and dispersion state during cycling. Such dynamic change, which is not typically accessible under  
53 steady-state catalytic conditions, can play a crucial role in enabling efficient CO<sub>2</sub> conversion at  
54 relatively low temperatures.

55 Although RWGS-CL offers substantial advantages in principle, significant gaps still remain for it to  
56 be realised as an economically viable process. In particular, increasing the product formation rate and  
57 shortening the cycle time are priority research challenges for improving the feasibility of chemical  
58 looping processes.<sup>10</sup> One effective approach to enhancing productivity is the development of high-  
59 performance OCs, particularly in terms of redox capacity and kinetics. As OCs for RWGS-CL, a wide  
60 variety of materials have been proposed, including composite oxides based on Fe<sup>11,12</sup>, In<sup>13,14</sup>, and Ga<sup>15</sup>,  
61 as well as oxygen-nonstoichiometric oxides such as perovskites<sup>4,16-18</sup> and CeO<sub>2</sub>.<sup>19,20</sup> Furthermore,  
62 previous studies have demonstrated that supporting these materials on high-surface-area supports can  
63 significantly enhance the performance of OCs.<sup>21-30</sup> The introduction of support material is considered



64 to improve key properties of OCs, including pore volume, surface area, and resistance to sintering,  
65 thereby enhancing their productivity. By appropriately combining redox-active species with suitable  
66 support materials, there is considerable potential to develop OC materials with more advanced and  
67 innovative performance.

68 In this study, a series of Co-In-based OCs supported on various oxides were prepared and their  
69 RWGS-CL performances were systematically compared. Among the OCs screened, 20wt%  
70 CoIn<sub>2</sub>/CeO<sub>2</sub> exhibited superior performance, its structure and reaction mechanism were investigated  
71 in detail. The redox behaviour and reaction kinetics were evaluated using fixed-bed reactor tests, the  
72 structural and electronic states of the OCs were investigated by electron microscopy, and *in-situ* X-ray  
73 absorption fine structure (XAFS) and *in-situ* X-ray diffraction (XRD) measurements.

## 75 2. Experimental

### 76 2.1 Material preparation

77 In this study, oxygen carriers (OCs) containing 15.9wt% In and 4.1wt% Co on a metal-weight basis,  
78 corresponding to 1.38 mmol of In and 0.69 mmol of Co per gram of OC, were prepared by  
79 impregnation with CeO<sub>2</sub> (JRC-CEO-1, supplied by the Catalysis Society of Japan) as the support. First,  
80 CeO<sub>2</sub> and 20 mL of distilled water were placed in a 200 mL round-bottom flask and stirred under  
81 reduced pressure at 120 rpm for 30 min using a rotary evaporator. Subsequently, In(NO<sub>3</sub>)<sub>3</sub>·*n*H<sub>2</sub>O  
82 (Kanto Chemical Co. Inc.) and Co(NO<sub>3</sub>)<sub>2</sub>·6H<sub>2</sub>O (Kanto Chemical Co. Inc.), used as metal precursors,  
83 were dissolved in distilled water and added to the same flask, followed by further reduced-pressure  
84 stirring for 20 min. The solvent was then gradually evaporated under reduced pressure using a water  
85 bath. After partial removal of water, the slurry was transferred to an evaporating dish and dried to  
86 completeness by heating on a hot stirrer. The resulting solid was dried overnight at 393 K in an oven  
87 and then calcined in a muffle furnace. Calcination was carried out by heating to 873 K at a ramp rate  
88 of 10 K min<sup>-1</sup> and holding for 5 h.

89 The prepared OC had a molar ratio of Co to In of 1:2, and because the total loading of Co and In  
90 corresponded to 20wt%, it is denoted as 20wt% CoIn<sub>2</sub>/CeO<sub>2</sub>. Using the same procedure, OCs supported  
91 on  $\gamma$ -Al<sub>2</sub>O<sub>3</sub> (JRC-ALO-6), SiO<sub>2</sub> (JRC-SIO-11), anatase-type TiO<sub>2</sub> (a-TiO<sub>2</sub>, JRC-TIO-7), and rutile-  
92 type TiO<sub>2</sub> (r-TiO<sub>2</sub>, JRC-TIO-16) were also prepared. All oxide supports used in this study were  
93 supplied by the Catalysis Society of Japan.

94 For performance comparison, a previously reported material (Co-In<sub>2</sub>O<sub>3</sub>) was prepared by impregnating



16.5wt% Co onto separately synthesised  $\text{In}_2\text{O}_3$ . The procedure was identical to the impregnation method described above, except that the calcination temperature was 773 K.  $\text{In}_2\text{O}_3$  was prepared by a citric-acid complex polymerisation method.  $\text{In}(\text{NO}_3)_3 \cdot n\text{H}_2\text{O}$  was used as the precursor and dissolved in distilled water together with citric acid and ethylene glycol (Kanto Chemical Co. Inc.), each added in a threefold molar ratio, in a Teflon beaker. The resulting solution was heated to 573 K and stirred with a hot stirrer to evaporate the solvent to dryness. The obtained solid was then subjected to two-step calcination in a muffle furnace, consisting of pre-calcination at 673 K for 10 h followed by final calcination at 1123 K for 10 h.

## 2.2 Isothermal RWGS-CL tests

Isothermal RWGS-CL tests were carried out at atmospheric pressure using a fixed-bed flow reactor. The reaction temperature was maintained at 773 K, and the total gas flow rate was set to  $100 \text{ mL min}^{-1}$ . First, the reactor was heated from room temperature to 773 K at a heating rate of  $20 \text{ K min}^{-1}$  under an Ar flow. After reaching the target temperature, the reduction step was conducted by flowing 10vol%  $\text{H}_2$  diluted in Ar for 15 min. In the subsequent oxidation step, 10vol%  $\text{CO}_2$  diluted in Ar was supplied until no further CO formation was detected. One sequence consisting of the reduction and oxidation steps was defined as one RWGS-CL cycle. The produced CO was detected and quantified using a quadrupole mass spectrometer (QIC-20, Hiden Analytical). OC particles sieved to a size range of 0.355 to 0.5 mm were packed into a quartz reactor tube (outer diameter 8 mm, inner diameter 6 mm) with a weight of 0.15 g. The amount of CO produced during the oxidation step was quantified using a calibration curve, and the following evaluation metrics were calculated.

- (1) Amount of CO produced (mmol): the integrated amount of CO generated during the oxidation step.
- (2) CO yield ( $\text{mmol g}^{-1}$ ): the value in (1) divided by 0.15 and normalised to amount of CO produced per 1 g of OC.
- (3) Oxidation completion time (s): defined as the time point at which the instantaneous CO formation rate, calculated from the temporal variation of the mass spectrometric signal and expressed in  $\text{mmol g}^{-1} \text{ h}^{-1}$ , decreased below  $2 \text{ mmol g}^{-1} \text{ h}^{-1}$ .
- (4) Space-time yield of CO (STY,  $\text{mmol g}^{-1} \text{ h}^{-1}$ ): calculated by dividing (2) by (3), representing the space-time yield of CO generated during the oxidation step.
- (5) Overall  $\text{CO}_2$  conversion during the complete oxidation cycle: defined as the ratio of the total



126 amount of CO produced to the total amount of CO<sub>2</sub> supplied during the oxidation completion time.  
127 (6) Reduction degree: defined as the ratio of the amount of CO produced to the amount of oxygen  
128 available in the oxygen carrier. For Co–In<sub>2</sub>O<sub>3</sub>, the theoretical amount of oxygen was calculated to be  
129 9.02 mmol g<sup>-1</sup>. Accordingly, for the oxygen carriers containing 20wt% CoIn<sub>2</sub>, the maximum oxygen  
130 release from In<sub>2</sub>O<sub>3</sub> was estimated to be 2.08 mmol g<sup>-1</sup>, and this value was used to calculate the  
131 reduction degree for  $\gamma$ -Al<sub>2</sub>O<sub>3</sub> and SiO<sub>2</sub> supported samples. For TiO<sub>2</sub>- and CeO<sub>2</sub>-supported samples, the  
132 available oxygen amount was experimentally determined by TG-DTA measurements under 10vol%  
133 H<sub>2</sub> at 500 °C for up to 120 min, and this value was used for the calculation of the reduction degree.

134  
135 In the present experimental setup, accurate quantification of H<sub>2</sub>O formation during the reduction step  
136 was technically challenging. Therefore, the CO yield defined in Eq. (2) is also treated as an indicator  
137 of the reduction rate. RWGS-CL cycle tests conducted using thermogravimetric analysis confirmed  
138 that all OCs investigated in this study are capable of regenerating nearly 100% of the lattice oxygen  
139 released during the reduction step in the subsequent oxidation step (in Figure S1). Accordingly, the  
140 amount of CO produced in the flow reactor experiments can be regarded as equivalent to the amount  
141 of oxygen reduced during the reduction step. Because the reduction time was fixed when comparing  
142 the performance of different OCs, the relative magnitude of the CO yield can be considered to reflect  
143 the relative reduction rates of the OCs.

144 The CO<sub>2</sub> conversion during the oxidation step was measured using the same reactor system. After  
145 heating under the same conditions, the OC was reduced in the reduction step using 50vol% H<sub>2</sub> for 30  
146 min. Prior to the oxidation step, the total gas flow rate was adjusted under Ar flow to match the CO<sub>2</sub>  
147 flow rate used in the subsequent oxidation step. Then, 100vol% CO<sub>2</sub> was supplied at a prescribed flow  
148 rate until oxidation was completed. The sample weight was fixed at 1.00 mg.

149 The CO<sub>2</sub> conversion was calculated using the following equation:

$$\text{CO}_2 \text{ conversion [\%]} = \frac{F_{\text{CO}}}{F_{\text{CO}_2} + F_{\text{CO}}} \times 100$$

151 where  $F_{\text{CO}}$  and  $F_{\text{CO}_2}$  represent the molar flow rates of CO and CO<sub>2</sub> at the reactor outlet, respectively,  
152 in units of mol min<sup>-1</sup>.

### 154 2.3 Characterisation

155 X-ray diffraction (XRD) measurements were performed to evaluate the crystalline structures of the  
156 OC samples. Measurements were carried out using a SmartLab III diffractometer (Rigaku Corp.)



157 operated at 40 kV and 40 mA with Cu K $\alpha$  radiation. Diffraction patterns were collected over a  
158 range of 10 to 90 degrees with a scanning rate of 5 degrees min<sup>-1</sup>.

159 Specific surface areas were determined by the Brunauer-Emmett-Teller (BET) method using nitrogen  
160 adsorption isotherms. Measurements were conducted with a Gemini VII instrument (Micromeritics  
161 Instrument Corp.). Prior to measurement, the samples were pretreated at 473 K for 1 h under a N<sub>2</sub>  
162 atmosphere.

163 Transmission electron microscopy (TEM) observations and energy-dispersive X-ray spectroscopy  
164 (EDS) mapping were performed using a field-emission transmission electron microscope (HF-2200,  
165 Hitachi) and a scanning transmission electron microscope with an energy-dispersive X-ray  
166 spectrometer (STEM-EDX, JEM 2100F (UHR); JEOL).

167 To evaluate the electronic states and coordination environments of metal species during the RWGS-  
168 CL reaction, transmission-mode *in-situ* XAFS measurements were conducted at the In *K*-edge and Ce  
169 *K*-edge. Measurements were performed at the BL14B2 beamline of the SPring-8 in Japan. *In-situ* XRD  
170 measurements were conducted simultaneously. Disc-shaped pellets of OC powder were used as  
171 samples. The samples were first heated from room temperature to 773 K under a He atmosphere.  
172 Subsequently, 50vol% H<sub>2</sub> was introduced and flowed for 10 min. The gas was then switched to He,  
173 and XAFS and XRD measurements were carried out. This sequence of reduction and measurement  
174 was repeated until no further changes were observed in the XANES spectra. Next, 10vol% CO<sub>2</sub> was  
175 introduced under the same conditions and flowed for 1 min. As in the reduction step, the gas was then  
176 switched to He and measurements were performed. This sequence was repeated until no further  
177 changes were observed in the XANES spectra. In all steps, the total gas flow rate was maintained at  
178 100 mL min<sup>-1</sup>. For XAFS measurements, transmission-mode XAFS was performed using two  
179 ionisation chambers. Quick-scan mode was employed, with a measurement time of 500 s per scan. For  
180 XRD measurements, a flat-panel detector was used as a two-dimensional detector. The camera length  
181 was set to 481.5 mm, the X-ray energy during XRD measurements was 27.9 keV, and the exposure  
182 time was 180 s. The obtained data, expressed in terms of the scattering vector *q*, were converted to  
183 equivalent diffraction patterns corresponding to Cu K $\alpha$  radiation using the equation described below,  
184 and the converted spectra are presented in this study.

$$185 \quad 2\theta_{\text{Cu}} = 2 \sin^{-1} \left( \frac{q\lambda_{\text{Cu}}}{4\pi} \right)$$

186 Here,  $\lambda_{\text{Cu}}$  denotes the wavelength of Cu K $\alpha$  radiation.

187



### 3. Results & Discussion

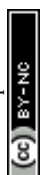
#### 3.1 RWGS-CL performance of supported Co-In<sub>2</sub>O<sub>3</sub>

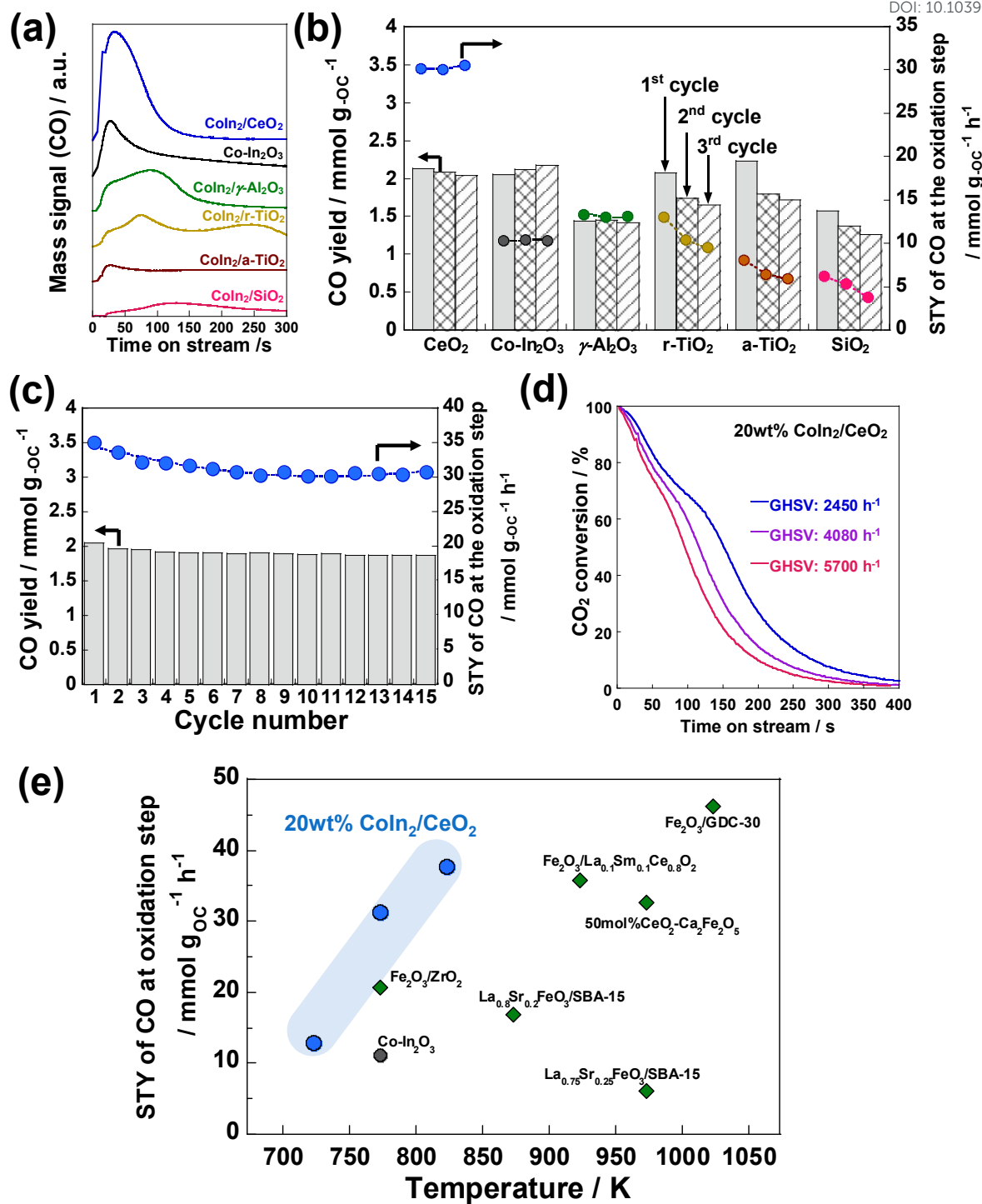
188 Isothermal RWGS-CL cycling tests were conducted to compare the performance of OC materials  
189 consisting of 20wt% CoIn<sub>2</sub> supported on various oxides with that of unsupported Co-In<sub>2</sub>O<sub>3</sub>. Figure 1  
190 and Table S1 summarise the CO production performance during the oxidation step of the OCs.  
191 Unsupported Co-In<sub>2</sub>O<sub>3</sub> itself exhibited an average CO yield of 2.11 mmol g<sup>-1</sup> and a space-time yield  
192 (STY) of 11.2 mmol g<sup>-1</sup> h<sup>-1</sup> over three cycles. The performance of the supported CoIn<sub>2</sub> OCs varied  
193 significantly depending on the oxide supports. For r-TiO<sub>2</sub>, a-TiO<sub>2</sub> and SiO<sub>2</sub>, both the CO yield and  
194 STY were lower than those of unsupported Co-In<sub>2</sub>O<sub>3</sub>, while  $\gamma$ -Al<sub>2</sub>O<sub>3</sub> showed only a slightly higher  
195 STY. Considering that the amount of Co-In species in the supported oxides is one-fifth of that in Co-  
196 In<sub>2</sub>O<sub>3</sub>, normalisation of the performance with respect to the amount of CoIn<sub>2</sub> reveals that, as shown in  
197 Table S1, these supported OCs exhibited higher CO yield and STY than Co-In<sub>2</sub>O<sub>3</sub>. This indicates that  
198 both the reduction and oxidation rates of the Co-In species were enhanced in these supported OCs.  
199 However, the extent of this enhancement was insufficient to compensate for the decreased amount of  
200 Co-In species. In contrast, 20wt% CoIn<sub>2</sub>/CeO<sub>2</sub> showed markedly enhanced performance, achieving a  
201 CO yield of 2.08 mmol g<sup>-1</sup>, comparable to that of Co-In<sub>2</sub>O<sub>3</sub>, and an STY of 31.2 mmol g<sup>-1</sup> h<sup>-1</sup>, which  
202 is approximately three times that of Co-In<sub>2</sub>O<sub>3</sub>. Figure 1c and Table S3 present the results of a  
203 continuous 15-cycle RWGS-CL test conducted to evaluate the performance stability of 20wt%  
204 CoIn<sub>2</sub>/CeO<sub>2</sub>. Although both the CO yield and STY gradually decreased up to the seventh cycle, they  
205 subsequently stabilised at approximately 2 mmol g<sup>-1</sup> and 30 mmol g<sup>-1</sup> h<sup>-1</sup>, respectively. In terms of  
206 the key functions required for OC materials, namely CO yield, CO space-time yield, and durability,  
207 20wt% CoIn<sub>2</sub>/CeO<sub>2</sub> exhibited superior performance. To examine the possible influence of carbon  
208 formation under the present reaction conditions, Raman spectra were conducted for the CoIn<sub>2</sub>/CeO<sub>2</sub>  
209 before and after RWGS-CL operation. As shown in Figure S3, no characteristic bands corresponding  
210 to carbon species (i.e., D and G bands in the range of 1200–1750 cm<sup>-1</sup>) were observed, including those  
211 after reduction, oxidation, and stability tests. These results indicate that carbon deposition is negligible  
212 under the present conditions. Therefore, the CO production behaviour discussed above is not affected  
213 by carbon formation.

214 From the perspective of practical implementation of the RWGS-CL process, OCs that can maintain  
215 a high CO<sub>2</sub> conversion during the oxidation step are particularly desirable, as this would reduce the  
216 separation and recovery burden associated with unreacted CO<sub>2</sub>. Accordingly, the temporal evolution  
217  
218

219 of CO<sub>2</sub> conversion during the oxidation step was evaluated for Co-In<sub>2</sub>O<sub>3</sub> and 20wt% CoIn<sub>2</sub>/CeO<sub>2</sub>. In  
220 this evaluation, 1 g of the OC was reduced in 50vol% H<sub>2</sub> for 60 min, followed by exposure to 100vol%  
221 CO<sub>2</sub> supplied at a prescribed flow rate. Figures 1d, S4 and Table S4 show the results obtained for Co-  
222 In<sub>2</sub>O<sub>3</sub> and CoIn<sub>2</sub>/CeO<sub>2</sub>. For unsupported Co-In<sub>2</sub>O<sub>3</sub>, the CO<sub>2</sub> conversion decreased exponentially from  
223 approximately 80% immediately after the start of the oxidation step, and the overall CO<sub>2</sub> conversion  
224 in this test was a maximum of 9.5%. In contrast, CoIn<sub>2</sub>/CeO<sub>2</sub> exhibited an initial CO<sub>2</sub> conversion of  
225 approximately 100%, and the conversion behaviour gradually approached a step-function-like,  
226 sigmoid profile as the GHSV was decreased. Under these conditions, the overall CO<sub>2</sub> conversion  
227 reached a maximum of 20.6%. For achieving high efficiency in the RWGS-CL process, it is ideally  
228 desirable that the CO<sub>2</sub> conversion exhibits step-function-type behaviour, allowing a high outlet CO  
229 concentration to be maintained while preserving a high space-time yield. As described above,  
230 CoIn<sub>2</sub>/CeO<sub>2</sub> is capable of splitting CO<sub>2</sub> with a very high rate, and therefore is considered able to  
231 maintain a relatively high conversion even under a high-concentration CO<sub>2</sub> feed. Based on this series  
232 of performance evaluations, it is evident that CeO<sub>2</sub> is uniquely effective as a support material for  
233 Co-In<sub>2</sub>O<sub>3</sub>.

234 Figure 1e and Table S5 compare the performance of 20wt% CoIn<sub>2</sub>/CeO<sub>2</sub> with previously reported  
235 OCs<sup>14,21–30</sup> for RWGS-CL in terms of reaction temperature and STY. 20wt% CoIn<sub>2</sub>/CeO<sub>2</sub> exhibits  
236 remarkably high STY values in a relatively low reaction temperature range of 723 to 823 K, and can  
237 therefore be regarded as a highly promising OC material in comparison with previously reported  
238 systems.





239

240 Figure 1 (a) Mass signal of CO ( $m/z = 28$ ). (b) CO production amount and the space-time yield of CO241 on the prepared OCs at the oxidation step. (c) Performance of CO production on 20wt%  $\text{CoIn}_2/\text{CeO}_2$ 242 during the stability test. (d)  $\text{CO}_2$  conversion on 20wt%  $\text{CoIn}_2/\text{CeO}_2$  during the oxidation step using243 100vol%  $\text{CO}_2$ . (e) Comparison of 20wt%  $\text{CoIn}_2/\text{CeO}_2$  to other reported supported-type oxygen carriers

244 for RWGS-CL.

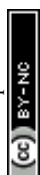
245



### 3.2 Structural characteristics and redox mechanism of Co-In supported CeO<sub>2</sub>

Table S6 summarises the BET specific surface areas of the Co-In supported OCs in the as-prepared, after the reduction step, and after the oxidation step. The data for post-reaction were obtained from samples that were cooled to room temperature under an Ar flow after experiencing each step at 773 K, followed by removal from the reactor. All CoIn<sub>2</sub>-supported OCs exhibited higher specific surface areas than unsupported Co-In<sub>2</sub>O<sub>3</sub>, both in the as-prepared and after reaction, indicating that an increase in surface area was achieved by supporting. An interesting observation is that CoIn<sub>2</sub>/CeO<sub>2</sub>, which exhibited the highest RWGS-CL performance, possessed the lowest specific surface area among the supported OCs. Therefore, the performance shown in Table S1 cannot be explained by differences in the specific surface area. Figure 2a shows the EDX mapping images of 20wt% CoIn<sub>2</sub>/CeO<sub>2</sub> (as-prepared, after reduction and oxidation of 3<sup>rd</sup> RWGS-CL cycle). In the as-prepared 20wt% CoIn<sub>2</sub>/CeO<sub>2</sub>, both In and Co were heterogeneously distributed on the CeO<sub>2</sub> support. In contrast, after the reduction step, the mapping images of In and Ce almost completely overlapped, indicating that the In species became uniformly dispersed over the CeO<sub>2</sub> surface. Although some localised regions of Co were still observed, Co was also relatively widely distributed. Following re-oxidation, the overall dispersion of In is largely maintained, although locally aggregated regions can be observed (highlighted by dashed lines). These observations suggest that the dispersion of In species on CeO<sub>2</sub> is significantly improved through the RWGS-CL cycles, while some local heterogeneity remains. The partial aggregation of In after re-oxidation is likely associated with the oxidation of metallic In to In<sub>2</sub>O<sub>3</sub>, which is also supported by the *in-situ* XRD observations discussed later. The localisation of Co became more pronounced. These results indicate that the supported In species on 20wt% CoIn<sub>2</sub>/CeO<sub>2</sub> were highly dispersed under RWGS-CL cycling conditions.

To further investigate the redox mechanism of 20wt% CoIn<sub>2</sub>/CeO<sub>2</sub>, *in-situ* XRD and XAFS measurements were performed. Figure S5 shows the XRD patterns recorded during RWGS-CL cycling at 773 K, while Figures 2b and 2c present magnified views of the regions of interest. During the reduction step under a 50vol% H<sub>2</sub> atmosphere, the intensity of In<sub>2</sub>O<sub>3</sub> (ICDD: 00-021-0406) decreased, accompanied by the appearance of diffraction peaks attributable to intermetallic compounds such as CoIn<sub>2</sub> (ICDD: 01-091-6508) and CoIn<sub>3</sub> (ICDD: 00-041-0880), although their intensities were relatively low. During the subsequent oxidation step under a 10vol% CO<sub>2</sub> atmosphere, these intermetallic phases disappeared, and In<sub>2</sub>O<sub>3</sub> and metallic Co (ICDD: 01-089-4307) were observed. This behaviour indicates that In<sub>2</sub>O<sub>3</sub> was reduced by H<sub>2</sub>, followed by alloying between metallic In and



277 Co, and that CoIn alloys were subsequently oxidised by CO<sub>2</sub> and separated into metallic Co and In<sub>2</sub>O<sub>3</sub>.  
278 In addition, analysis of the diffraction peak width and intensity provides further insight into the  
279 structural evolution during RWGS-CL cycling. The diffraction peak corresponding to CeO<sub>2</sub> (111)  
280 shows little change in both width and intensity throughout the redox cycles, indicating that the CeO<sub>2</sub>  
281 support maintains its structure under the present reaction conditions. In contrast, the diffraction peaks  
282 attributed to In<sub>2</sub>O<sub>3</sub> after the oxidation step become broader and less intense compared to those of the  
283 as-prepared sample. This change suggests a decrease in crystallite size and an increase in the dispersion  
284 of In<sub>2</sub>O<sub>3</sub> species upon RWGS-CL cycling. It should be noted that no distinct amorphous fraction was  
285 observed in the XRD patterns of CoIn<sub>2</sub>/CeO<sub>2</sub>. This indicates that the material remains predominantly  
286 crystalline under the present conditions.

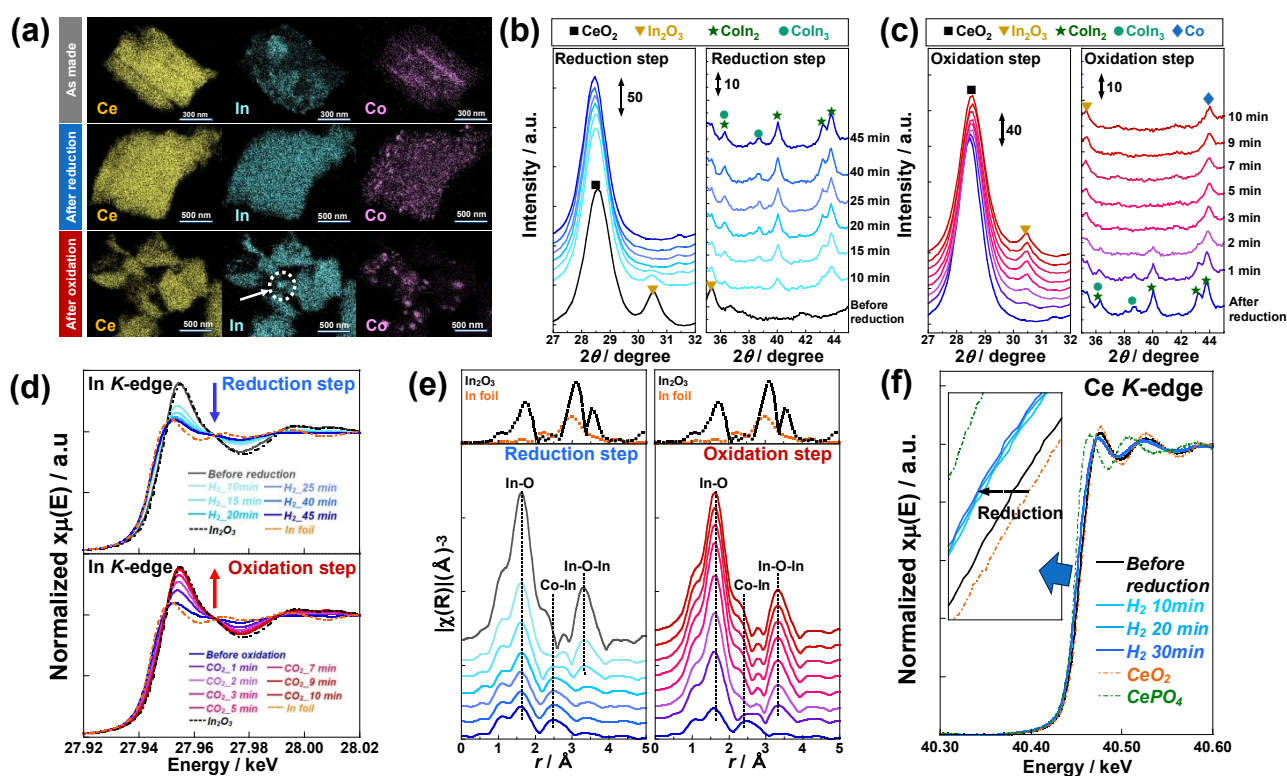
287 The XRD patterns of the other supported OCs exhibited broadly similar behaviour (Figure S6). In the  
288 as-prepared, diffraction peaks corresponding to the support oxides and In<sub>2</sub>O<sub>3</sub> were observed. After the  
289 reduction step, the In<sub>2</sub>O<sub>3</sub> decreased or disappeared, accompanied by the appearance of CoIn<sub>2</sub>.  
290 Following the oxidation step, the CoIn<sub>2</sub> phase disappeared, while intense diffraction peaks of In<sub>2</sub>O<sub>3</sub>  
291 and metallic Co appeared. These results suggest that the redox of In species accompanied by the  
292 formation and decomposition of CoIn alloys occurred for all OCs. This behaviour is consistent with  
293 the redox mechanism of Co-In<sub>2</sub>O<sub>3</sub> reported in our previous study.<sup>14</sup> In contrast, analysis of the  
294 diffraction peak width and intensity indicates that a different structural evolution occurs compared to  
295 CoIn<sub>2</sub>/CeO<sub>2</sub>. For all samples, the diffraction peaks attributed to In<sub>2</sub>O<sub>3</sub> after the oxidation step become  
296 significantly more intense and sharper compared to those of the as-prepared state. This indicates an  
297 increase in crystallite growth of In<sub>2</sub>O<sub>3</sub> during RWGS-CL cycling on these supports, suggesting that In  
298 species tend to aggregate and form larger crystalline domains.

299 Notably, the diffraction intensities of the intermetallic compounds observed for 20wt% CoIn<sub>2</sub>/CeO<sub>2</sub>  
300 were relatively small compared with those for other OCs with the same loading of Co and In,  
301 suggesting that these phases existed on the support in a highly dispersed state. In addition, as shown  
302 in Figure 2a, Co exhibited a localisation greater than In after the reduction step, implying that some In  
303 species may not be alloyed with Co. Focusing on the CeO<sub>2</sub> (111) diffraction peak, a shift towards lower  
304 angles during the reduction and towards higher angles during the oxidation was observed. This  
305 behaviour reflects changes in the lattice volume associated with the release and regeneration of lattice  
306 oxygen in CeO<sub>2</sub>, suggesting that the CeO<sub>2</sub> support itself also undergoes redox during RWGS-CL cycle.

307 The *in-situ* XAFS results shown in Figures 2d–f are in good agreement with the *in-situ* XRD



308 observations. Figure 2d shows the temporal evolution of the In *K*-edge XANES spectra during the  
 309 reduction and oxidation steps. The spectrum before reduction closely matched that of the reference  
 310  $\text{In}_2\text{O}_3$  sample, indicating that In was initially in the  $\text{In}^{3+}$  state. Under an  $\text{H}_2$  atmosphere, the white-line  
 311 intensity gradually decreased with time, and the spectral shape evolved towards that of In foil,  
 312 indicating the reduction of  $\text{In}_2\text{O}_3$  to metallic In species. The XANES spectrum after reduction did not  
 313 share an isosbestic point with the reference samples (Figure S7), and therefore linear combination  
 314 fitting was not applied, most likely due to the contribution of CoIn alloy species formed during  
 315 reduction. Upon switching to a  $\text{CO}_2$  atmosphere, the XANES spectra rapidly returned to a state  
 316 comparable to that before reduction, indicating reoxidation of the In species by  $\text{CO}_2$ . In the EXAFS  
 317 spectra, a peak emerged at approximately  $2.5 \text{ \AA}$  as the reduction progressed. Since this peak did not  
 318 correspond to In-In scattering, it is attributed to CoIn alloy formation. The Ce *K*-edge XANES spectra  
 319 shown in Figure 2f indicate a slight reduction of  $\text{Ce}^{4+}$  under the reduction step, which is also consistent  
 320 with the *in-situ* XRD results.



321 Figure 2 (a) EDX mapping images of 20wt%  $\text{CoIn}_2/\text{CeO}_2$  before and after RWGS-CL cycle. *In-situ*  
 322 XRD results of 20wt%  $\text{CoIn}_2/\text{CeO}_2$  under (c) 50vol%  $\text{H}_2$  (reduction step) and (d) 10vol%  $\text{CO}_2$   
 323 (oxidation step) at 773 K. (d) In *K*-edge XANES spectra of 20wt%  $\text{CoIn}_2/\text{CeO}_2$  under 50vol%  $\text{H}_2$   
 324 (reduction step) and 10vol%  $\text{CO}_2$  (oxidation step) at 773 K. (e) In *K*-edge EXAFS spectra of 20wt%



326 CoIn<sub>2</sub>/CeO<sub>2</sub> under 50vol% H<sub>2</sub> (reduction step) and 10vol% CO<sub>2</sub> (oxidation step) at 773 K. (f) Co K  
 327 edge XANES spectra of 20wt% CoIn<sub>2</sub>/CeO<sub>2</sub> under 50vol% H<sub>2</sub> (reduction step) at 773 K.  
 328

View Article Online  
 DOI: 10.1039/C6EE01452A

### 3.3 Evaluation of the roles of individual components in CoIn<sub>2</sub>/CeO<sub>2</sub>

329 To clarify the roles of the individual components, namely Co, In, and CeO<sub>2</sub>, in the high RWGS-CL  
 330 performance of CoIn<sub>2</sub>/CeO<sub>2</sub>, a series of comparative studies was conducted. Figures S8–S9, Tables 1  
 331 and S7 summarise the RWGS-CL performance of 15.9wt% In/CeO<sub>2</sub>, 4.1wt% Co/CeO<sub>2</sub>, and bare CeO<sub>2</sub>,  
 332 together with that of 20wt% CoIn<sub>2</sub>/CeO<sub>2</sub>. The loadings of In and Co were adjusted to match those in  
 333 20wt% CoIn<sub>2</sub>/CeO<sub>2</sub>.  
 334

335  
 336 Table 1 Performance for the prepared OCs (20wt% CoIn<sub>2</sub>/CeO<sub>2</sub>, 15.9wt% In/CeO<sub>2</sub>, 4.1wt% Co/CeO<sub>2</sub>  
 337 and CeO<sub>2</sub>).

Oxygen carrier	CO production /mmol	CO yield / mmol g <sup>-1</sup>	Reduction degree / %	Oxidation completion time /s	Space-time yield / mmol g <sup>-1</sup> h <sup>-1</sup>	Overall CO <sub>2</sub> conversion / %
20wt% CoIn <sub>2</sub> /CeO <sub>2</sub>	0.313	2.08	83.3	240	31.2	17.5
15.9wt% In/CeO <sub>2</sub>	0.219	1.46	73.1	146	36.0	20.2
4.1wt% Co/CeO <sub>2</sub>	0.011	0.07	-	77	3.5	1.9
CeO <sub>2</sub>	0.011	0.07	-	65	4.0	2.3

338  
 339 Focusing first on the bare CeO<sub>2</sub>, the CO yield was only 0.07 mmol g<sup>-1</sup>, indicating a very limited  
 340 contribution. Although CeO<sub>2</sub> itself undergoes redox, its direct contribution to CO formation is  
 341 considered to be minor. In contrast, 15.9wt% In/CeO<sub>2</sub> exhibited a CO production of 1.46 mmol g<sup>-1</sup>  
 342 and a remarkably high STY of 36.0 mmol g<sup>-1</sup> h<sup>-1</sup>, clearly indicating that In species act as the primary  
 343 redox-active species and the active sites for CO<sub>2</sub> splitting. STEM-EDX images of reduced 15.9wt%  
 344 In/CeO<sub>2</sub> (Figure S10) show that, similar to 20wt% CoIn<sub>2</sub>/CeO<sub>2</sub>, the In species on CeO<sub>2</sub> are highly  
 345 dispersed. Figure 3 compares the XRD patterns of CoIn<sub>2</sub>/Al<sub>2</sub>O<sub>3</sub> and CoIn<sub>2</sub>/CeO<sub>2</sub> after multiple RWGS-  
 346 CL cycles. For CoIn<sub>2</sub>/Al<sub>2</sub>O<sub>3</sub>, the crystallite size of In<sub>2</sub>O<sub>3</sub> increased with increasing cycle number,  
 347 indicating that aggregation of In and Co species easily progresses on the Al<sub>2</sub>O<sub>3</sub> surface. Comparison  
 348 of the EDX mapping images of CoIn<sub>2</sub>/Al<sub>2</sub>O<sub>3</sub> shown in Figure S11 with those of CoIn<sub>2</sub>/CeO<sub>2</sub> in Figure  
 349 2a clearly reveals aggregation of the In species. In contrast, for CoIn<sub>2</sub>/CeO<sub>2</sub>, the crystallite size of In<sub>2</sub>O<sub>3</sub>  
 350 decreased with increasing cycle number. ICP results (Table S8) show that the amount of supported In



351 remained nearly unchanged even after multiple cycles. Therefore, the decrease in  $\text{In}_2\text{O}_3$  crystallite size  
352 cannot be attributed to the loss of In species through volatilisation, but rather indicates dispersion of  
353 In species on  $\text{CeO}_2$  surface during RWGS-CL cycle. To further clarify the evolution of the dispersion  
354 state during RWGS-CL cycling, additional EDX mapping images after 1 cycle and after 15 cycles  
355 have been provided in Figures S12 and S13. Comparison of these results with the 3-cycle data shown  
356 in Figure 2a indicates that In species become significantly dispersed already during the first cycle.  
357 Although slight local aggregation of In species is observed after the oxidation step, the overall  
358 dispersion is largely maintained throughout the cycling. This suggests that such aggregation is partially  
359 reversed during the subsequent reduction step through oxygen release, leading to dispersion of In  
360 species on  $\text{CeO}_2$  and suppressing excessive aggregation. Furthermore, the dispersion of In species  
361 tends to improve with increasing cycle number. This behaviour is consistent with the XRD analysis  
362 shown in Figure 3, where the gradual decrease in crystallite size suggests progressive dispersion of In  
363 species during RWGS-CL operation. These results demonstrate that  $\text{CeO}_2$  plays a crucial role in  
364 inducing spontaneous high dispersion of In species and suppressing their aggregation under reaction  
365 conditions through strong metal-support interactions. To further elucidate the origin of this support-  
366 dependent dispersion behaviour, XPS analysis was conducted for  $\text{CoIn}_2/\text{CeO}_2$  and  $\text{CoIn}_2/\text{Al}_2\text{O}_3$  before  
367 and after RWGS-CL cycling. These results are shown in Figure S14. For  $\text{CoIn}_2/\text{CeO}_2$ , the In3d peak  
368 exhibited a shift of approximately 0.5 eV toward higher binding energy after cycling, whereas no  
369 noticeable shift was observed for  $\text{CoIn}_2/\text{Al}_2\text{O}_3$ . This result indicates that the electronic state of In  
370 species is modified specifically on the  $\text{CeO}_2$  support, suggesting a interaction between In species and  
371  $\text{CeO}_2$ <sup>31</sup>. Considering the redox properties of  $\text{CeO}_2$  and its ability to form oxygen vacancies, such  
372 interaction may contribute to the spontaneous dispersion of In species under RWGS-CL conditions.



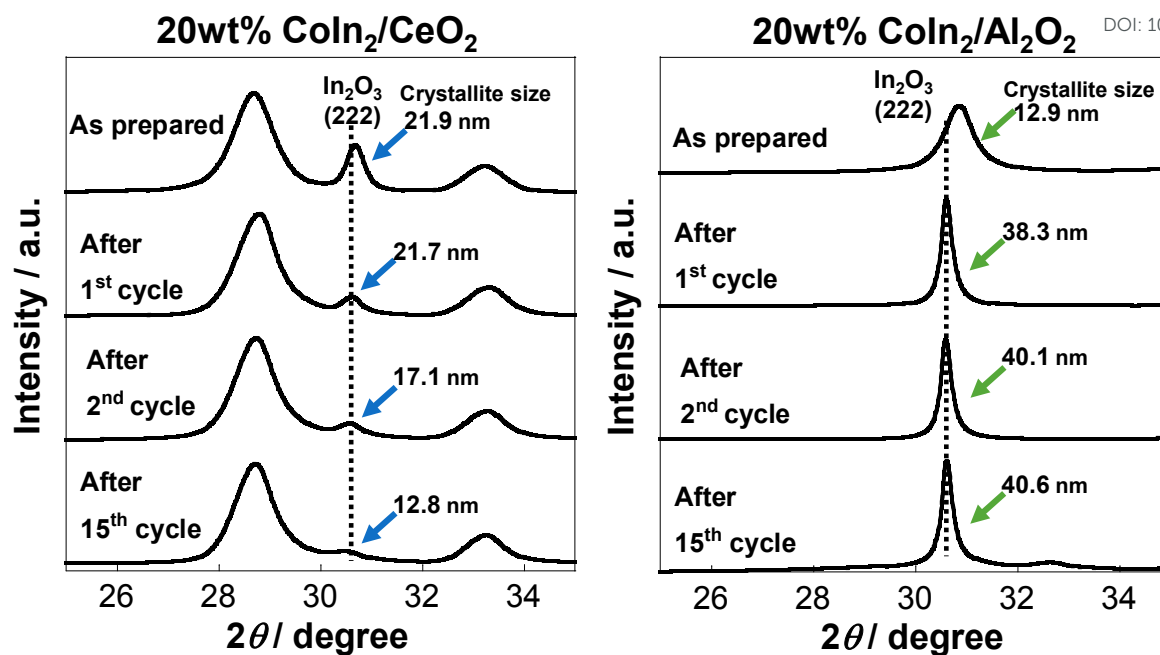


Figure 3 Crystallite size of In<sub>2</sub>O<sub>3</sub> on XRD patterns for CoIn<sub>2</sub>/CeO<sub>2</sub> and CoIn<sub>2</sub>/Al<sub>2</sub>O<sub>3</sub>.

Next, the role of Co was examined. As evidenced by *in-situ* XRD, metallic Co was observed even after the oxidation step, indicating that Co undergoes little redox under RWGS-CL conditions at 773 K. Accordingly, the CO yield on 4.1wt% Co/CeO<sub>2</sub> was nearly identical to that on bare CeO<sub>2</sub>. However, the CO yield on 20wt% CoIn<sub>2</sub>/CeO<sub>2</sub> was approximately 1.4 times higher than that of 15.9wt% In/CeO<sub>2</sub>. Since the amount of CO produced during the oxidation step corresponds to the amount of In reduced during the preceding reduction step, Co is considered to enhance the reduction rate of supported In species. Figure 4a and Tables S9–S10 compare the RWGS-CL performance of OCs with varying Co to In ratios. Regardless of the amount of supported Co, the CO yield was consistently approximately 2 mmol g<sup>-1</sup>, indicating that even a small amount of Co provides a comparable enhancement effect. To clarify whether Co contributes to the dispersion of In species, additional STEM-EDX mapping images of In/CeO<sub>2</sub> (without Co) before and after oxidation are provided in Figure S15. In the as-prepared sample, In species exhibit a clearly inhomogeneous distribution, whereas after oxidation, they become relatively well dispersed on the CeO<sub>2</sub> support. Combined with the EDX results after the reduction step shown in Figure S11, these observations indicate that the dispersion of In species occurs on CeO<sub>2</sub> even in the absence of Co. Therefore, Co does not contribute to the dispersion of In species.

To further elucidate the role of Co, kinetic analyses based on the Hancock-Sharp method<sup>32–34</sup> were performed. The experimental data used for fitting the reaction models were obtained by thermogravimetric analysis. The weight loss observed under a 10vol% H<sub>2</sub> flow was assumed to



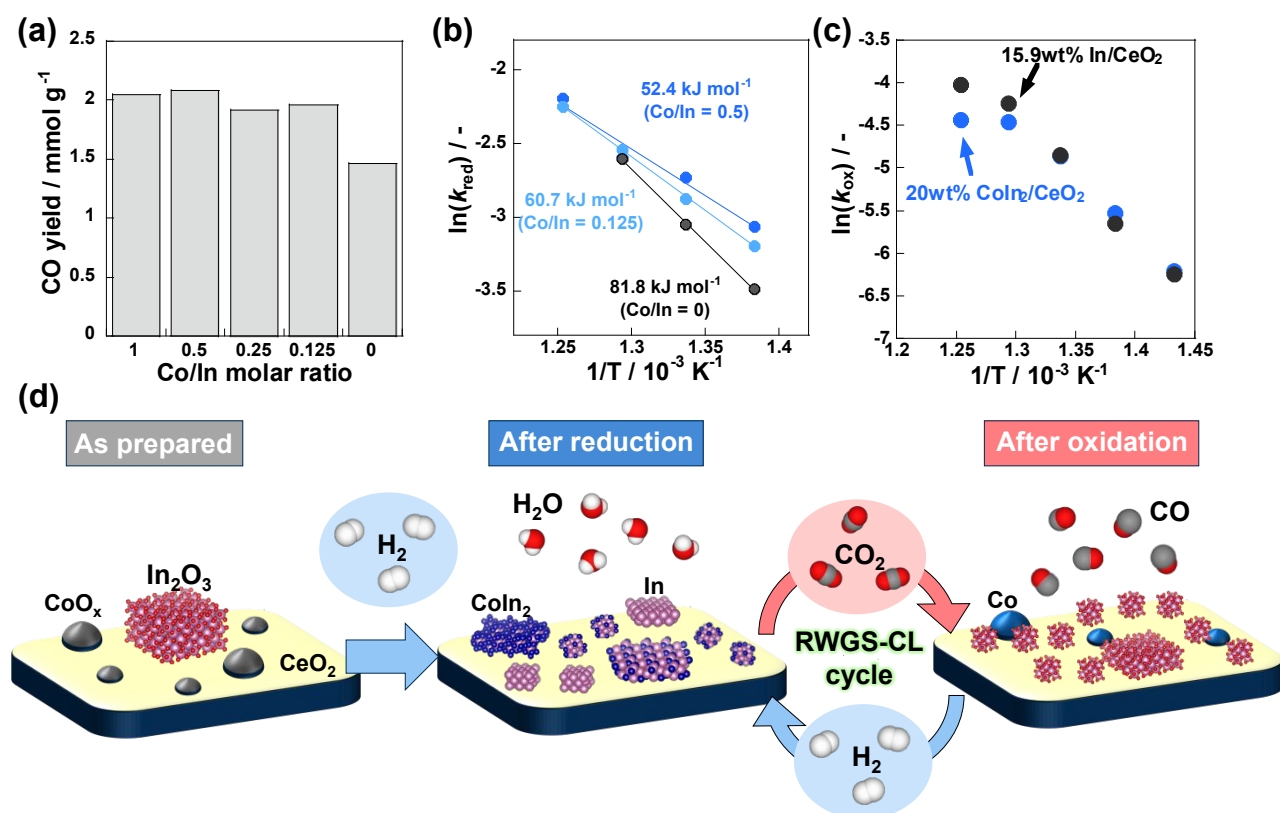
394 correspond to oxygen released from the OCs, and the reduction degree of each OC was calculated  
395 accordingly. Figure S16 shows the fitting results of the model reaction rate equations to the  
396 experimental data. For all OC materials, the Avrami-Erofe'ev nucleation-and-growth model<sup>35–37</sup>  
397 provided the best fit to the experimental data for all OC materials. Arrhenius plots constructed using  
398 the obtained rate constants  $k_{\text{red}}$  are shown in Figure 4b. The apparent activation energy of In/CeO<sub>2</sub>  
399 without Co (Co/In = 0) was 81.8 kJ mol<sup>-1</sup>, whereas CoIn<sub>8</sub>/CeO<sub>2</sub> (Co/In = 0.125) and CoIn<sub>2</sub>/CeO<sub>2</sub> (Co/In  
400 = 0.5) exhibited values approximately 21–29 kJ mol<sup>-1</sup> lower. This enhancement in the reducibility of  
401 In species is attributed to promoted H<sub>2</sub> dissociation on metallic Co particles and subsequent H spillover  
402 to surface In species. The promotion of In<sub>2</sub>O<sub>3</sub> reduction via H spillover mediated by metal  
403 nanoparticles such as noble metals<sup>38</sup>, Ni<sup>39</sup>, and Co<sup>40</sup> has been widely reported. The series of  
404 CoIn<sub>x</sub>/CeO<sub>2</sub> investigated here possessed sufficient Co loading and surface distribution to supply  
405 dissociated hydrogen to surface In species at a sufficiently high rate, resulting in a Co-loading-  
406 independent enhancement effect.

407 Kinetic analysis of the oxidation step was also conducted using the Hancock-Sharp method (Figures  
408 4c and S17). As expected, the rate constants  $k_{\text{ox}}$  were nearly identical regardless of the presence or  
409 absence of Co. Therefore, Co in CoIn<sub>2</sub>/CeO<sub>2</sub> primarily contributes to enhancing the reaction rate of  
410 the reduction step, whereas the high CO formation rate during the oxidation step is mainly attributed  
411 to the dramatically increased contact frequency between CO<sub>2</sub> and highly dispersed In species.

412 Figure 4d schematically illustrates the structural features and reaction mechanism of Co-In supported  
413 CeO<sub>2</sub> OC materials, including 20wt% CoIn<sub>2</sub>/CeO<sub>2</sub>. In the as-prepared state, Co and In are present as  
414 oxide species that are sparsely and heterogeneously distributed on the CeO<sub>2</sub> surface. Upon exposure  
415 to an H<sub>2</sub> atmosphere during the reduction step, both Co and In are reduced to their metallic states,  
416 accompanied by the formation of Co-In alloys such as CoIn<sub>2</sub>. Metallic Co functions as an active site  
417 for H<sub>2</sub> dissociation, thereby promoting the reduction of In species via hydrogen spillover.  
418 Simultaneously, dispersion of In species occurs, leading to the formation of CeO<sub>2</sub> surface uniformly  
419 covered with In species. During the subsequent oxidation step, the metallic In species and Co-In alloys  
420 react with CO<sub>2</sub> to produce CO, while In is selectively reoxidised to In<sub>2</sub>O<sub>3</sub>. Notably, the In species  
421 remain highly dispersed without excessive aggregation, leading to a surface structure in which sparsely  
422 distributed metallic Co nanoparticles coexist with uniformly dispersed In<sub>2</sub>O<sub>3</sub>. Thereafter, RWGS-CL  
423 cycling proceeds through the redox of highly dispersed In species on the CeO<sub>2</sub>. The high dispersion of  
424 In species is considered to increase the contact frequency with CO<sub>2</sub>, resulting in an enhanced CO



425 formation rate. An additional advantage of Co-In supported  $\text{CeO}_2$  is that such spontaneous dispersion  
 426 is induced under RWGS-CL reaction conditions, enabling preparation by a simple impregnation  
 427 method without the need for elaborate structural design of the support material. This effective  
 428 utilisation of metal-support interactions represents a promising strategy for the rational design of  
 429 advanced OC materials.



31  
 32 Figure 4 (a) CO yield of  $\text{CoIn}_x/\text{CeO}_2$  with different Co/In ratios. (b) Arrhenius plots and apparent  
 433 activation energies for the reduction step. (c) Arrhenius plots for the oxidation step. (d) Schematic  
 434 illustration of the structural features and redox mechanism of  $\text{CoIn}_2/\text{CeO}_2$ .

#### 436 4. Conclusion

437 In this study, the performance of indium-based oxygen carriers supported on various oxides was  
 438 systematically investigated for the RWGS-CL process. Among the OCs examined,  $\text{CoIn}_2/\text{CeO}_2$   
 439 exhibited simultaneously high CO yield and space-time yield, and stable performance. A notable  
 440 experimental observation was that In species supported on  $\text{CeO}_2$  underwent spontaneous dispersion  
 441 under reaction conditions, whereas such behaviour was not observed on the other oxide supports



442 examined. This dispersion behaviour resulted in a highly dispersed In surface during RWGS-CL  
443 operation, which is considered to contribute to the enhanced CO formation rate through increased  
444 contact frequency with CO<sub>2</sub>. In addition, the presence of Co was found to promote the reduction  
445 kinetics of the supported In species, likely via enhanced H<sub>2</sub> dissociation and hydrogen spillover, while  
446 having a negligible influence on the oxidation kinetics. This result demonstrates that the choice of  
447 support can critically influence the structural evolution of oxygen carriers under RWGS-CL cycle.  
448 These findings highlight the importance of considering support-induced dispersion behaviour in the  
449 design of RWGS-CL oxygen carriers and suggest that high-performance OCs can be realised by  
450 exploiting such effects using simple preparation methods such as impregnation.

### 52 **Author contributions**

53 Conceptualisation: TH and YS, funding acquisition: YS, investigation: TH, SI, KI, project  
54 administration: YS, supervision: YS, validation: TH, SI, KI, YS, visualization: TH, writing – original  
55 draft: TH, writing – review & editing: YS.

### 57 **Conflicts of interest**

58 There are no conflicts to declare.

### 60 **Data availability**

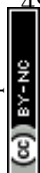
61 The data supporting this article have been included as part of the Supplementary Information

### 63 **Acknowledgements**

64 We appreciate Dr. Takeshi Watanabe (Japan Synchrotron Radiation Research Institute, SPring-8) for  
65 his great support with *in-situ* XAFS and XRD measurements in BL14B2 (proposal No. 2024B2102,  
66 2024B1974 and 2024B1036). Equipment (JEM-2100F: Material Characterization Central Laboratory  
67 in Waseda University) shared with the MEXT Project for Promoting Public Utilization of Advanced  
68 Research Infrastructure (Program for supporting the construction of core facilities) under grant number  
69 JPMXS0440500023 was used. A part of this work was supported by JST-ALCA-Next Program Grant  
70 Number 23836167, Japan, by JSPS KAKENHI 24H00487, 23H05404, 23K20034, Japan.

472 **References**

- 473 1 Climate Change 2021: The Physical Science Basis, Contribution of Working Group I to the Sixth  
474 Assessment Report of the Intergovernmental Panel on Climate Change.
- 475 2 S. J. Davis, K. Caldeira and H. D. Matthews, *Science* 2010, **329**, 1330–1333.
- 476 3 B. Dziejarski, R. Krzyżyńska, K. Andersson, *Fuel*, 2023, **342**, 127776.
- 477 4 Y. A. Daza, J. N. Kuhn, *RSC Advances*, 2016, **6**, 49675–49691.
- 478 5 M. L. T. Triviño, N. C. Arriola, Y. S. Kang, J. G. Seo, *Chemical Engineering Journal*, 2024, **487**,  
479 150369.
- 480 6 W. Zhang, J. Sun, H. Wang, X. Cui, *Chemistry – An Asian Journal*, 2024, **19**, e202300971.
- 481 7 Y. A. Daza, R. A. Kent, M. M. Yung, J. N. Kuhn, *Industrial Engineering & Chemistry Research*  
482 2014, **53**, 14, 5828–5837.
- 483 8 M. Wenzel, L. R.-Struckmann, K. Sundmacher, *AIChE Journal*, 2017, **63**, 1, 15–22.
- 484 9 K. Kang, H. Sampei, Y. Sekine, *RSC Sustainability*, 2025, **3**, 1598-1628.
- 485 10 J.-P. Lange, V.L. Sushkevich, A.J. Knorpp, J. A. v. Bokhoven, *Industrial Engineering & Chemistry*  
486 *Research* 2019, **58**, 8674–8680.
- 487 11 Y. Qiu, L. Ma, D. Zeng, M. Li, D. Cui, Y. Lv, S. Zhang, R. Xiao, *Journal of Energy Chemistry*,  
488 2020, **46**, 123–132.
- 489 12 L. Ma, Y. Qiu, M. Li, D. Cui, S. Zhang, D. Zeng, R. Xiao, *Industrial Engineering & Chemistry*  
490 *Research*, 2020, **59**, 6924–6930
- 491 13 J. Makiura, T. Higo, Y. Kurosawa, K. Murakami, S. Ogo, H. Tsuneki, Y. Hashimoto, Y. Sato, Y.  
492 Sekine, *Chemical Science*, 2021, **12**, 2108–2113.
- 493 14 J. Makiura, S. Kakihara, T. Higo, N. Ito, Y. Hirano, Y. Sekine, *Chemical Communications* 2022,  
494 **58**, 4837–4840.
- 495 15 K. Kang, S. Kakihara, T. Higo, H. Sampei, K. Saegusa, Y. Sekine, *Chemical Communications*,  
496 2023, **59**, 11061–11064.
- 497 16 H. Z. Shi, V. R. Bhethanabotla, J. N. Kuhn, *Journal of CO<sub>2</sub> Utilization*, 2021, **51**, 101638.
- 498 17 A. E. Ramos, D. Maiti, Y. A. Daza, J. N. Kuhn, V. R. Bhethanabotla, *Catalysis Today*, 2019, **338**,  
499 52–59.
- 500 18 Y. Goto, K. Yamazaki, M. Kikugawa, M. Aoki, *Dalton Transactions*, 2024, **53**, 13847–13853.
- 501 19 T. Higo, K. Saegusa, S. Ishizaki, S. Kakihara, Y. Yayama, Y. Hirano, Y. Sekine, *Journal of Physical*  
502 *Chemistry C*, 2025, **129**, 44, 19786-19793.



- 503 20 F. J. Pomiro, G. G. Fouga, A. E. Tamietti, A. E. Bohé, G. D. Micco, *Chemical Engineering Journal*,  
504 2024, **498**, 155222.
- 505 21 E. Sun, G. Wan, V. Haribal, J. Rojas, R. Gupta, A. Majumdar, *Cell Reports Physical Science* 2025,  
506 **4**, 9, 101581.
- 507 22 A. Jo, Y. Kim, H.S. Lim, M. Lee, D. Kang, J.W. Lee, *Journal of CO<sub>2</sub> Utilization* 2022, **56**, 101845.
- 508 23 B.J. Hare, D. Maiti, Y.A. Daza, V. R. Bhethanabotla, J.N. Kuhn, *ACS Catalysis* 2018, **8**, 4, 3021–  
509 3029.
- 510 24 B. Jin, H. Poelman, C. Detavernier, Z. Liang, G. B. Marin, V. V. Galvita, *Applied Catalysis B:  
511 Environmental*, 2021, **292**, 120194–120204.
- 512 25 J. Zhao, Y.W. Xiong, Z.H. Gao, F.Y. Fu, L.L. Niu, M. Jin, *Sustainable Energy & Fuels*, 2022, **6**,  
513 5, 1448-1457.
- 514 26 J.C. Brower, B.J. Hare, V.R. Bhethanabotla, J.N. Kuhn, *ChemCatChem* 2020, **12**, 24, 6317-6328.
- 515 27 Z. Sun, K. Lei, L.R. Smith, N.F. Dummer, R.J. Lewis, H. Qi, K.J. Aggett, S.H. Taylor, Z. Sun, G.J.  
516 Hutchings, *Carbon Energy* 2025, **7**, 9, e70011.
- 517 28 D. Zeng, Y. Qiu, L. Ma, M. Li, D. Cui, S. Zhang, R. Xiao *Environmental Science & Technology*  
518 2020, **54**, 19, 12467–12475.
- 519 29 N.V.R.A. Dharanipragada, L.C. Buelens, H. Poelman, E.D. Grave, V.V. Galvita, G.B. Marin  
520 *Journal of Materials Chemistry A*, 2015, **3**, 16251.
- 521 30 L. C. Buelens, A. Dharanipragada, H. Poelman, Z. Zhou, G. B. Marin and V. V. Galvita, *Journal  
522 of CO<sub>2</sub> Utilization*, 2019, **29**, 36.
- 523 31 X. Liu, K. Wang, D. Cao, C. Li, L. Wang, M. Wang, Q. Li, C. Wu, K. Liu, *Fuel*, 2024, **362**, 30760
- 524 32 J. D. Hancock, J. H. Sharp, *Journal of the American Ceramic Society* 1972, **55**, 74-77.
- 525 33 K. Piotrowski, K. Mondal, H. Lorethova, L. Stonawski, T. Szymański, T. Wiltowski, *International  
526 journal of hydrogen energy* 2005, **30**, 1543-1554.
- 527 34 Z. Zhou, L. Han and G. M. Bollas, *International journal of hydrogen energy* 2014, **39**, 8535-8556.
- 528 35 M. Avrami, *The Journal of chemical physics* 1939, **7**, 1103-1112.
- 529 36 M. Avrami, *The Journal of chemical physics* 1940, **8**, 212-224.
- 530 37 M. Avrami, *The Journal of chemical physics* 1941, **9**, 177-184.
- 531 38 N. Rui, Z. Wang, K. Sun, J. Ye, Q. Ge, C.-J. Liu, *Applied Catalysis B: Environmental* 2017, **218**,  
532 488-497.
- 533 39 Y. Cai, C. Lin, X. Cha, Y. Wu, X. Rao, K. B. Tan, D. Cai, G.-L. Zhuang, G. Zhan, *ACS Catalysis*



534 2024, **14**, 11, 8463–8479.

View Article Online  
DOI: 10.1039/D6SE00152A

535 40 M. Zhang, H. Chen, Ka. Cheng, L. Zhao, H. Huang, J. Kang, Q. Zhang, Y. Wang, *The Journal of*  
536 *Physical Chemistry C* 2025, **129**, 5, 2535–2545.



## 1 **Data availability**

View Article Online  
DOI: 10.1039/D6SE00152A

2 The data supporting this article have been included as part of the Supplementary Information

